Soil Dynamics and Earthquake Engineering 92 (2017) 109–121

Contents lists available at ScienceDirect

Soil Dynamics and Earthquake Engineering

journal homepage: www.elsevier.com/locate/soildyn

System identification and modal analysis of an arch dam based on earthquake response records

Jian Yang[a,*,1], Feng Jin[b], Jin-Ting Wang[b], Li-Hang Kou[c]

[a] Huaneng Clean Energy Research Institute, 102209 Beijing, China
[b] State Key Laboratory of Hydroscience and Engineering, Tsinghua University, 100084 Beijing, China
[c] China Guodian Corporation, 100034 Beijing, China

ARTICLE INFO

Keywords:
Arch dam
Seismic record
Modal properties
System identification
Finite element modal analysis

ABSTRACT

The true dynamic characteristics of dams, namely, natural frequencies, damping ratios, and mode shapes, are important to earthquake-resistant design. Thus, system identification based on in-site measurements is useful for numerical analysis and health monitoring. The well-instrumented strong motion array on an arch dam in Southwestern China recorded some seismic response data. The dynamic properties of the dam are identified from records of the top five strongest earthquake motions using power spectral density functions, transfer functions, and the ARX model. The identified modal parameters of the different seismic events are compared, and the stability of the stiffness of the dam system from 2002 to 2008 and the nonuniformity in the input ground motion are indicated. A linear finite element model of the dam and a nonlinear model that considers contraction joints are constructed and calibrated to reproduce the frequencies determined from the system identification. The modal analysis highlights potential information about the dynamic characteristics of the dam. The comparison of the results of the system identification and calibration shows that the use of the nonlinear model may be reasonable in simulating the dynamic response of the Ertan Dam.

1. Introduction

The merit of strong motion records lies in the abundant information on the recurrence and characteristics of earthquakes and structural dynamic nonlinearity. However, the strong motion records of arch dams that have experienced earthquakes are very limited. Some of the important earthquake records of arch dams in the literature are shown in Table 1. Given that existing observational databases are insufficient, the studies based on the databases of actual dams are few.

Hall [1] summarized the development of the study on the dynamic and earthquake behavior of concrete dams by reviewing the literature; the resulting summary described actual earthquake observations, the experiments performed on prototype or model dams, and the analytical investigations into the dynamic properties of dams. The author also discussed the effect of different factors on the dynamic response of dams, including damping, water depth, water compressibility, and transverse joints. Fanelli et al. [2,3] presented the dynamic behavior of the Talvacchia Arch Dam in Italy in forced vibration tests and earthquake records and investigated the influence of environmental conditions (water level and temperatures) and the structural characteristics of the dam dynamic response. The study reported the phenomenon in which resonant frequencies initially increase with rising water level and then decrease with a further rise, as well as subsequent studies [4–10]. This phenomenon is usually attributed to the comprehensive effects of the added mass from water pressure, stiffness change (opening and closing of contraction joints), and damping ratio. Loh et al. [4,5] investigated the dynamic characteristics of the Fei-Tsui Dam during seismic events and ambient vibration tests using an autoregressive exogenous (ARX) model. The results showed that the damping ratio of the Fei-Tsui dam from the strong motion input (about 9–14%) was greater than the results of ambient tests (2–3%). The author also pointed out that the damping ratio of the Fei-Tsui dam increases with the increasing natural frequency of the system. Darbre [11] presented the basic principles of strong motion instrumentation schemes for dams and emphasized the recording of the free field motions at dam sites, the effective motions at abutments, and global dam responses. Then, he estimated and compared the dynamic properties of five Swiss dams (Grande Dixence, Mauvoisin, Punt dal Gall, Emosson, and Mattmark) during earthquakes with power spectral density (PSD) functions and transfer functions (TF) [12]. The results implied that the simple identification techniques are not well suited to a comprehensive identification of the dynamic characteristics of dams. Proulx

* Corresponding author.
E-mail address: yangjian@hnceri.com (J. Yang).
[1] The main part of this work was performed as a doctoral student in Tsinghua University by the corresponding author.

http://dx.doi.org/10.1016/j.soildyn.2016.09.039
Received 18 August 2015; Received in revised form 5 September 2016; Accepted 25 September 2016

Table 1
Selected strong motion records of arch dams in the world.

Name	Region	Completion	Height/m	Earthquake	Epicentral distance/km	Magnitude	Peak acceleration[a]	Water level[b] /m	Remarks
Longyangxia [18]	China	1990	178	1990/04/26	68	6.8	0.04*g*		The peak acceleration is recorded at abutment.
				1994/08/14	5.7	3.2	0.017*g*		
				1994/10/10	60	5.3	0.005*g*		
Shapai [21]	China	2003	132	2008/05/12	36	8.0		−1.5	Slight damage
Techi [1]	Taiwan, China		181	1986/11/15			0.167*g*		
Fei-Tsui [4,5]	Taiwan, China	1987	122.5	1994/06/05	43	6.2	0.032*g*	−19	
				1999/09/21		7.3	0.136*g*	−23	
Pacoima [1,16]	USA	1928	113	1971/02/09	5	6.6	1.25*g*	−45	A section of upper left abutment rock slid, and the joint between the dam and thrust block opened almost 1 cm. The peak acceleration is recorded at a ridge on the left abutment about 15 m above the dam crest.
				1994/01/17	18	6.8	2.0*g*	−40	The upper left abutment rock slid again. The joint at the thrust block opened 5 cm at the crest. A few cracks were observed. The peak acceleration is obtained along the abutments near the crest.
				2001/01/13	6	4.3	0.16*g*	−41	No damage
Big Tujunga [1]	USA	1931	77	1971/02/09	32	6.6	0.25*g*	−29	No damage. The peak acceleration is recorded at abutment.
Santa Anita [1]	USA	1927	70	1971/02/09	27	6.6	0.17*g*		No damage The peak acceleration is recorded at right abutment.
Tonoyama [1,22]	Japan	1957	64.5	1960/12/26	75	6.0	0.03*g*		No damage
Nagawado [1,23]	Japan	1970	155	1984/09/14	37	6.8	0.247*g*	−24	
Ikehara [24]	Japan	1964	111	1995/01/17	106	7.2	0.082*g*		
Kurobe [1,22]	Japan	1963	186	1961/08/19	10	4.9	0.185*g*	−85	Concrete placement nearly complete. The peak acceleration is recorded at foundation rock.
				1972/09/08	8	3.9	0.116*g*		
Ambiesta [1,25]	Italy	1956	59	1976/05/06	22	6.5	0.33*g*		No damage. The peak acceleration is recorded at abutment.
Maina diSauris [25]	Italy	1952	136	1976/05/06	43	6.5			No damage
Barcis [25]	Italy	1955	50	1976/05/06	48	6.5			No damage
Talbacchia [1,26]	Italy	/	77	1986/11/25	250	5.5	0.13 cm/s	−25	No damage
Monteynard [25]	France	1962	155	1963/04/23	0	4.9			No damage
Kariba [25]	Zambia/ Zimbabwe	1956	128	1963/08/14–1963/11/08	0	6.1			Slight damage
				2010/08/31	45	5.5			No damage
Mauvoisin [12,14]	Switzerland	1957	250	1993/06/14	71	4.4	< 0.015*g*		
				1994/11/01	0		0.014*g*		
				1996/03/31	13	4.6	0.014*g*		
				1996/07/15	100	5.2			
Emosson [14]	Switzerland	1974	180	2001/02/23	10	3.6	0.07*g*		
Punt-dal-Gall [14]	Switzerland	1968	130	1999/12/29	12	4.9	0.08*g*		
Barossa [1,27]	Australia	1902	36	1954/03/01	45	5.5			Few cracks
Ceres [1,27]	South Africa	1950	30	1969/09/29	25	6.6			Few cracks and leakage
Rapel [1,27]	Chile	1968	112	1968/03/03		7.7	0.31*g*	0	Few cracks on the inner walls of the spillway intakes; minor damage on the power intakes.
Susqueda [27]	Spain	1968	135	1969/02/28		8.0			More seepage

[a] Generally it is the recorded peak acceleration at the dam crest.
[b] Water levels preceded by a minus are distances below the crest of the dam, i.e., a water level at −19 m is 19 m below the dam crest.

et al. [13,14] further studied the damping representation in the Emosson, Mauvoisin, and Punt dal Gall dams on the basis of recorded earthquakes. Bell et al. [15] identified the dynamic properties of the Paocima Dam during the 1994 Northridge earthquake using the time-varying Fourier spectra method. They reported that the dam principal modal frequencies shifted during different periods of high acceleration; this condition indicated a significant reduction in the stiffness of the dam system. The phenomenon was ascribed to nonlinearities such as joint opening and abutment movement in strong earthquakes. Alves et al. [16,17] also estimated modal properties of the Pacoima Dam from two seismic records (1994 Northridge and 13 January 2001 earthquakes) and forced vibration experiments; the results also revealed the presence of nonlinearity in the dam response. Through finite element analysis, the source of the nonlinear behavior was explained as the loss of stiffness in the abutment rock mass. The spatial variation of the ground motion across the free-field canyon surface was also studied. Zhang et al. [18] analyzed the system modal damping and natural frequencies of the Longyangxia Arch Dam with domain analysis and compared the modal characteristics between earthquakes and vibration experiments. Most of these studies showed that resonant frequencies are relatively reasonable, but other dynamic parameters, especially damping ratio and participation factors, show poor reliability and high sensitivity to input uncertainty. In addition, large amplitudes of accelerations caused by the topographic amplification effect during earthquakes have been widely observed [1,4,5,12,15–20].

In this paper, we report the results of the system identification and modal analysis performed in an arch dam in Southwestern China. The dam is well instrumented strong motion array with accelerographs. The strong-motion instrumentations recorded about 20 earthquake events from 2001 to 2008. We select and preprocess the top five strongest events to identify the natural frequencies of the dam with PSD functions and TFs. The ARX model with multiple input–single output (MISO) and multiple input–multiple output (MIMO) are also employed to extract detailed information on the dynamic characteristics of the dam. Then, a linear finite element model of the dam and a nonlinear model that considers the effect of contraction joints are calibrated respectively. The subsequent modal analysis indicates that the nonlinear model is more reasonable than the linear model in simulating the dynamic characteristics of the Ertan dam.

2. Arch dam and earthquake response records

2.1. The Ertan Dam and its strong-motion instrumentation

Located on Yalong River, in Sichuan Province, Southwestern China, the Ertan Dam is a concrete double-curvature arch dam with a height H_s=240 m (Fig. 1). It was constructed from 1995 to 2000. The crest of the dam is at an altitude of 1205 m above sea level. It consists of 39 monoliths for a total crest length of 775 m. The thickness of the crown cantilever decreases from 55.7 m at the base to 11 m at the crest. The water level in the reservoir, H, normally varies from 50 m below the crest in summer (EL. 1155 m) and 5 m below the crest in winter (EL. 1200 m).

Fig. 2 shows the array configuration of the two sets of strong-motion instrumentations in the dam, which includes six three-component and six unidirectional accelerographs [28]. Stations B01-1, B08-2, B34-1, and B39-1 are located near the dam–foundation rock interface; stations B01-1 and B08-2 are located at the left side of the canyon (viewed from the upstream); and stations B34-1 and B39-1 are located at the right side. Station B21-4 is located near the base of the crown cantilever with a height difference of 15 m. Stations B21-1 to B21-4 are located on a vertical plane of the crown cantilever. However, the dam lacks free-field instruments.

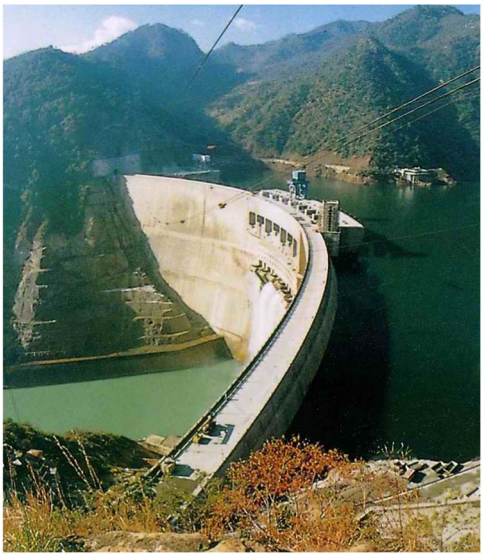

Fig. 1. Top view of the left abutment of the Ertan Arch Dam.

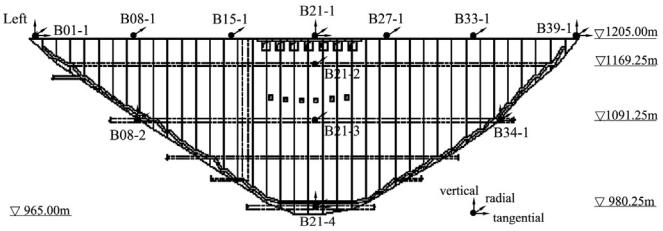

Fig. 2. Sketch of the array configuration of the strong-motion instrumentations.

2.2. Earthquake records

Operating since 2001, the strong-motion instrumentations in the dam have recorded about 20 earthquake events. The summary of the records of the top five strongest earthquake events is shown in Table 2. The radial component of motions recorded at the stations is shown in Fig. 3. Similar figures for the tangential and vertical components are not included in the paper for brevity. All the strong-motion instrumentations were excited during the PuGe earthquake event, whereas only a set of strong-motion instrumentation was excited during the other four events. The motions were not extremely strong, but the records provide useful data about the spatial variations of dam response. The fact that the amplitude of accelerations values recorded at Station B27-1 was relative lower than other accelerographs in PuGe, DaYao and YanYuan earthquake was possibly attributed to instrument malfunction. After an overall maintenance of the strong motion array in 2007, the performance of accelerograph B27-1 became normal in WenChuan event. Hence, records obtained at Station 27-1 during abovementioned three events were omitted in the subsequent analysis.

The peak acceleration of the station at the left part of the dam was always higher than that of the symmetric station at the right side of the dam during the PuGe earthquake. An interesting occurrence was the consistently high acceleration of the radial component of station B08-1 (the distance from the left abutment is about one-fifth of the crest length) during all the earthquakes. In particular, the peak acceleration of the radial component of station B08-1 during the PanZhiHua earthquake was significantly higher than that of the radial component of station B21-1, which is located on top of the crown cantilever. The same was observed in the Nagawado Arch Dam in Japan and the Ambiesta Arch Dam in Italy [1]. Hall [1] explained that this phenomenon may be due to strong antisymmetric responses. However, this work has not been extended thus far.

Table 2
Details of the top five strongest earthquake events recorded at the Ertan Dam.

Earthquake event	Date	Magnitude	Epicentral distance (km)	Max. water depth (m)	Peak crest acceleration (cm/s^2)	Duration time (s)
PuGe	2002/04/10	M 5.0	105	196.4	6.59	42
DaYao	2003/07/21	M 6.2	116	226.8	14.92	23
YanYuan	2003/08/21	M 5.8	83	228.5	3.78	29
WenChuan	2008/05/12	M 8.0	550	192.4	115.74	278
PanZhiHua	2008/08/31	M 5.6	57	231.7	682.17	81

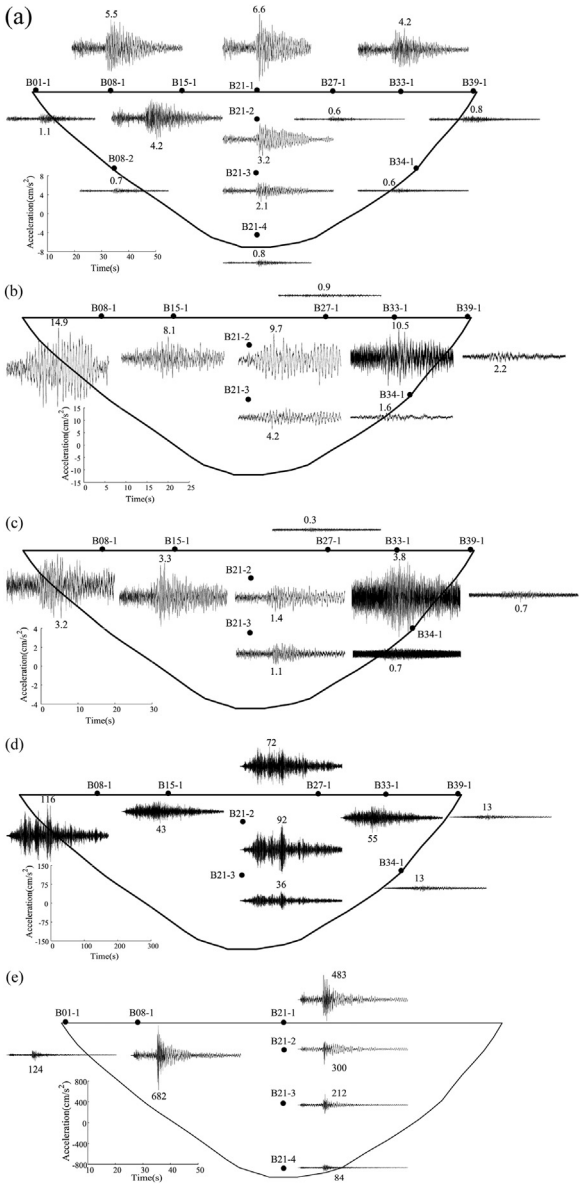

Fig. 3. Raw records of earthquakes in the radial direction: (a) PuGe earthquake event; (b) DaYao earthquake event; (c) YanYuan earthquake event; (d) WenChuan earthquake event; (e) PanZhiHua earthquake event; accelerations are in cm/s^2; the peak values are noted.

3. Identification of dynamic dam characteristics

The raw data of aforementioned records were preprocessed through filtering and base line correction before the identification and analysis of the dynamic properties of the Ertan Dam. The PSD functions and TF were initially calculated for every record of all the five earthquakes to identify the resonant frequencies of the dam. Then, the ARX model, proposed by Loh [4,5], was employed to extract information on the dynamic characteristics of the dam. The details on the ARX model are referred on Refs. [4,5].

Table 3
Identified resonant frequencies (Hz) from power spectral density functions during earthquakes.

Earthquake event	Records	Resonant frequencies					
		Item 1	Item 2	Item 3	Item 4	Item 5	Item 6
PuGe	B21-1/R	1.56	/	2.44/2.59	3.13	/	/
	B21-2/R	1.56	/	2.44	/	/	/
	B21-3/R	1.56	/	2.49	3.15	/	3.86
	B08-1/R	1.56	/	2.44	3.15	3.57	3.86
	B15-1/R	/	1.65	2.44	3.03	/	3.88
	B33-1/R	1.56	1.66	2.44	3.03	/	3.88
	Mean	1.56	1.66	2.46	3.10	3.57	3.87
DaYao	B08-1/R	1.42	1.51	2.25	/	3.42	3.71
	B15-1/R	/	1.51	2.25	2.88	3.42	3.61
	B21-2/R	1.42	1.56	/	/	/	/
	B21-3/R	1.42	1.56	/	/	3.42	/
	Mean	1.42	1.54	2.25	2.88	3.42	3.66
YanYuan	B08-1/R	1.46	2.34	/	3.61	4.10	4.49
	B15-1/R	1.46	2.34	2.83	3.61	4.10	4.49
	B21-2/R	1.46	2.25	/	3.61	4.10	/
	B21-3/R	1.46	2.34	/	3.71	4.10	/
	Mean	1.46	2.34	2.83	3.64	4.10	4.49
WenChuan	B08-1/R	1.59	1.66	2.44	/	/	/
	B15-1/R	/	1.68	2.44	3.08	3.88	4.76
	B27-1/R	1.59	1.68	2.44	/	3.88	/
	B33-1/R	1.59	1.68	2.44	3.08	3.88	/
	B21-2/R	1.59	/	2.44	/	/	/
	B21-3/R	1.59	/	2.55	/	/	/
	Mean	1.59	1.68	2.46	3.08	3.88	4.76
PanZhiHua	B08-1/R	1.42	1.49	2.32	/	2.93	3.44
	B21-1/R	1.42	1.49	/	/	/	/
	B21-1/T	/	1.51	/	/	/	/
	B21-2/R	1.42	1.49	2.20	/	/	/
	B21-3/R	1.42	1.49	2.34	2.59	2.93	3.42
	Mean	1.42	1.50	2.28	2.59	2.93	3.43

3.1. Dynamic properties identified from power spectral density functions

The resonant frequencies of the dam identified from the PSD functions of the five earthquake records are reported in Table 3. A half-power method was attempted to identify the damping ratios, but the method was not available in this case. The number of identified resonant frequencies was evidently different for every record of a certain earthquake event. Such difference implies the spatial motion of mode shapes. However, a certain corresponding resonant frequency from different records of the same event was consistent. Possibly because of the serious noise component of the records and the limitation of the PSD method, some resonant frequencies during the identification process might have been omitted or confused. The first two classes of resonant frequencies were particularly close that they nearly could not be clearly distinguished for most earthquakes.

Moreover, only a unique value could be recognized in the YanYuan earthquake. The first two classes of resonant frequencies were not always synchronously identified from the same record of an event. For example, the primary resonant frequency could not be extracted from the record of station B15-1 for the PuGe, DaYao, and WenChuan earthquakes. The second resonant frequency from the record of stations B21-1 and B08-1 for the PuGe earthquake could not be extracted as well. Thus the mode number could be hardily confirmed from the results computed by only one method. Even if the first two classes of resonant frequencies could be identified from a certain seismic record, the response power spectral density at the primary resonant frequency was generally considerably higher than that at the second frequency. It implied that the dynamic response of the dam at the primary resonant frequency was remarkably more intense than that at the second frequency in the earthquake.

3.2. Dynamic properties identified from transfer functions

Given the lack of seismic records near the dam–foundation rock interface, the TF of the records near the abutment and dam body was only applied for the PuGe and PanZhiHua earthquakes, as partly illustrated in Figs. 4 and 5, respectively. The frequency at which the coherence coefficient was not significant would be abnegated. The identified resonant frequencies from every record for the PuGe and PanZhiHua earthquakes are listed in detail in Tables 4 and 5, respectively. For the same input, the number of identified resonant frequencies varied with the different outputs during the same seismic event, and the TF amplitude varied at a certain frequency. For the same output, the number of identified resonant frequencies varied with the different inputs, and the TF amplitude varied at a certain frequency. This phenomenon revealed that the excitation of the different stations at the abutment made varied contributions to the response of the same station in the dam body. The dispersion of the identified resonant frequencies was generally wider than that obtained through the PSD method. The reason may be related to the serious noise component of the records and the low resolution of transfer function.

At the first identified resonant frequency, the amplitude of the TF between the record of the abutment station and the radial component of station B21-1, that is, the station on top of the crown cantilever, was slightly higher than that between the same abutment station and

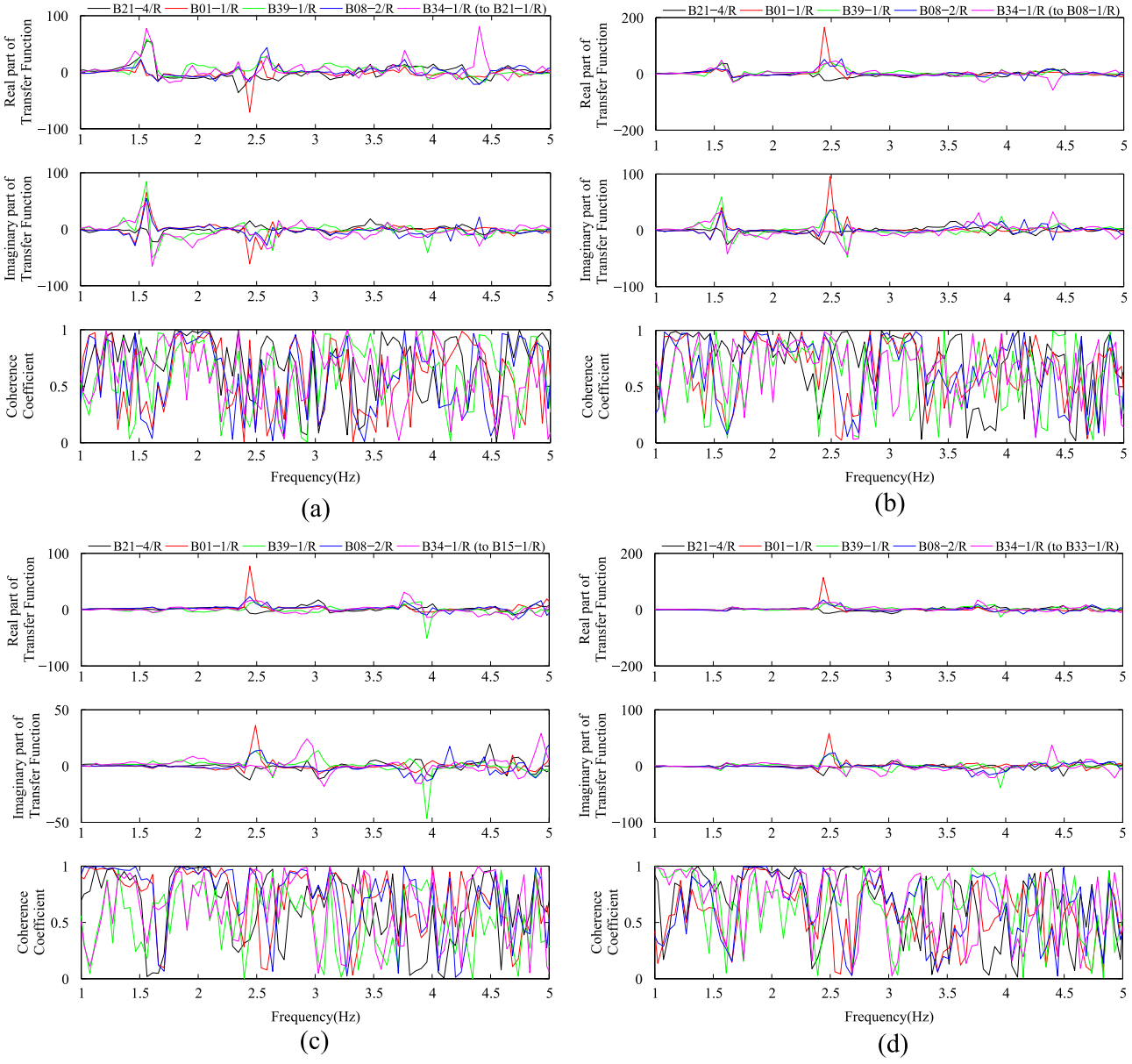

Fig. 4. Transfer functions with different outputs during the PuGe earthquake: (a) B21-1/R; (b) B08-1/R; (c) B15-1/R; (d) B33-1/R.

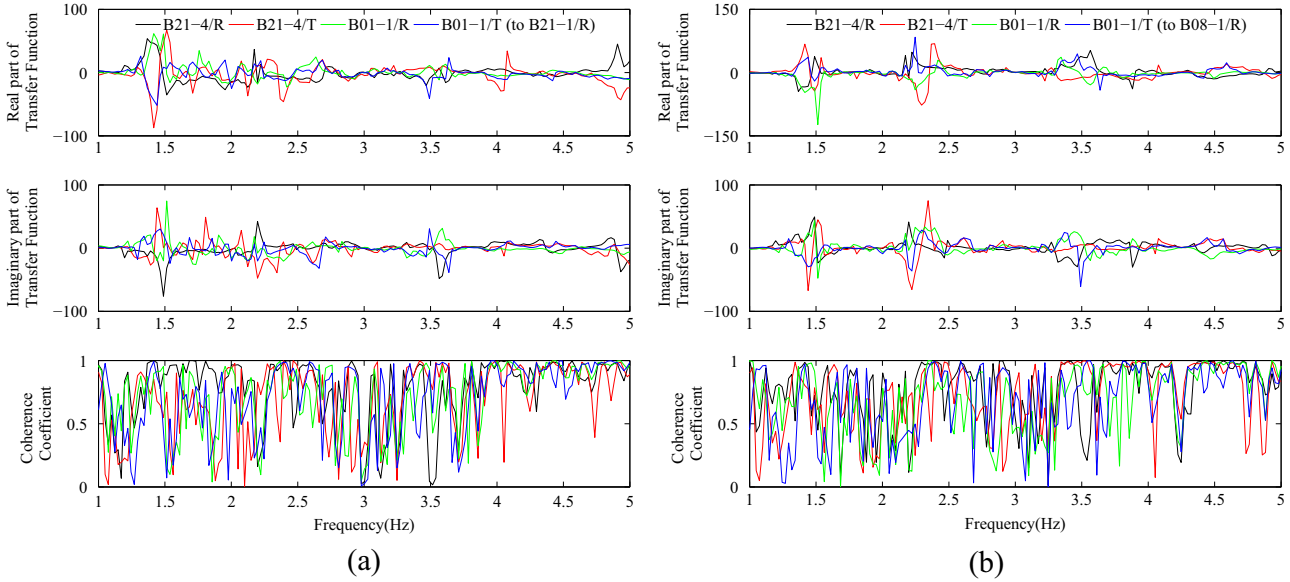

Fig. 5. Transfer functions with different outputs during the PanZhiHua earthquake: (a) B21-1/R; (b) B08-1/R.

station B08-1 during the PuGe and PanZhiHua events. The phase of the TF between the abutment station and the stations on the crown cantilever was the same with that between the same abutment station and station B08-1 during the PuGe event. However, the contrary phase was determined during the PanZhiHua event. This topic is discussed further in the next section.

At the second identified resonant frequency, the amplitude of most of the TFs between the record of the abutment station and the radial component of station B21-1 approached zero during the two earthquakes. In other words, the second-order frequency could not be extracted easily from these particular TFs. This phenomenon implied that nearly zero radial displacement existed at the crown cantilever in the second-order mode shape.

The TF between the records of different stations at the abutment is illustrated in Fig. 6. The low TF amplitude and the few resonant frequencies identified from the transfer functions implied non-uniform inputs from the abutment of the dam.

3.3. Dynamic properties identified with the ARX model

The ARX (MISO) model was utilized to identify the dynamic properties of the dam during the PanZhiHua earthquake. All the recorded motions along the abutment of the dam were used as input motions. In this way, the non-uniform inputs could be considered. The response of the radial component of the stations in the dam body was considered as an output. Then, the ARX (MIMO) model was employed to describe further the global behavior of the dam. The response data of the radial components of the stations located at the crest, namely, stations B21-1 and B08-1, were considered as outputs. The results obtained from the two models were consistent. The identified resonant frequencies and damping ratios are listed in Table 6. The identified frequency response functions from the ARX (MIMO) model are shown in Fig. 7. Further details are discussed as follows.

For the same input, the identified resonant frequencies from the frequency response functions with different outputs were consistent, although a slight difference could be determined. The amplitude of the estimated frequency response function also varied with different outputs. This observation can be attributed to the motion of the different stations of the dam body during the same seismic excitation. It was conducive to mode shape estimation. For example, the amplitude of the frequency response function of the radial component of station B21-1 at the second dominant frequency was extremely small, whereas that of the radial component of station B08-1 was quite clear. This finding indicated that the second dominant frequency could not be definitely identified from the record of the radial component of station B21-1 as well as with the TF method. Therefore, almost no radial displacement occurred at the crown cantilever in the second-order mode shape.

It is noted that the amplitude of the frequency response function for the same output was remarkably different with the different input during the same seismic event. The amplitude of the frequency response function with the record of station B21-4 as input during the PanZhiHua earthquake event was considerably larger than that with the record of station B01-1 as input. Such difference can be attributed to the fact that different inputs have different contributions to output responses. These results highlight the need to use a multiple input model to represent the non-uniform inputs along the abutment of the dam.

The phase difference in the frequency response function at the first identified resonant frequency for the outputs of the radial components of Stations B21-1 and B08-1 with the same input was approximately 180°. It implied that the radial motions at the two stations in the corresponding mode shape were opposite. Moreover, the phase of the frequency response function at the third identified resonant frequency for the outputs of the radial components of Stations B21-1 and B08-1 with the same input was equal. Hence, the radial motions at the two stations in the corresponding mode shape shared the same direction. This topic is discussed further in the next section.

Similar analysis with ARX model was performed for the other four earthquake events. The identified resonant frequencies and damping ratios are listed in Table 6.

3.4. Discussion of system identification

Despite the slight differences, the results of the system identification with different methods were generally consistent for a certain earthquake. Comparing among these results, the dynamic characteristics of the five seismic events are confirmed and listed in Table 6.

3.4.1. Resonant frequencies

The first three identified resonant frequencies could be definitely determined as the first three natural frequencies of the dam. The order of the subsequent identified resonant frequencies could not be determined because of possible frequency omission or confusion during the system identification. The first two order natural frequencies for the

Table 4
Resonant frequencies (Hz) identified via transfer functions for the PuGe earthquake.

Input	Output	Resonant frequencies					
		Item 1	Item 2	Item 3	Item 4	Item 5	Item 6
B21-4/R	B21-1/R	1.46	/	2.54	/	/	/
	B08-1/R	/	1.61	/	/	/	/
	B15-1/R	/	/	/	2.93	/	/
	B33-1/R	1.51	1.61	2.64	3.03	/	/
	B21-2/R	/	1.61	/	/	/	/
B21-4/T	B21-1/R	1.46	/	/	/	/	/
	B08-1/R	1.46	1.71	/	/	3.61	/
	B15-1/R	/	/	/	/	3.47	/
	B33-1/R	/	1.71	2.30	/	/	3.76
	B21-2/R	1.46	/	/	/	/	/
B01-1/R	B21-1/R	1.46	/	2.44	/	/	/
	B08-1/R	1.46	/	2.49	/	/	/
	B15-1/R	/	/	2.49	/	/	/
	B33-1/R	/	/	2.49	/	/	/
	B21-2/R	1.46	/	2.44	/	/	/
B01-1/T	B21-1/R	1.46	1.56	/	/	/	/
	B08-1/R	1.46	/	/	/	/	/
	B15-1/R	/	/	/	2.88	/	3.91
	B33-1/R	/	/	/	/	/	3.76
	B21-2/R	1.46	1.56	/	/	/	/
B39-1/R	B21-1/R	/	/	2.64	/	/	/
	B08-1/R	1.56	1.66	2.57	/	/	/
	B15-1/R	/	/	2.57	/	/	/
	B33-1/R	/	1.66	2.57	/	/	/
	B21-2/R	1.37	/	2.64	/	/	/
B39-1/T	B21-1/R	1.51	/	/	/	/	/
	B08-1/R	1.51	1.66	2.44	/	/	/
	B15-1/R	1.44	1.66	/	3.03	/	/
	B33-1/R	/	1.66	/	3.03	3.47	/
	B21-2/R	1.51	1.66	/	/	/	/
B08-2/R	B21-1/R	1.46	/	2.44	/	/	/
	B08-1/R	1.46	/	2.49	/	/	/
	B15-1/R	/	/	2.54	/	/	/
	B33-1/R	/	/	2.49	/	/	3.71
	B21-2/R	1.46	/	2.44	/	/	/
B08-2/T	B21-1/R	/	1.61	/	/	/	/
	B08-1/R	/	1.71	/	/	/	/
	B15-1/R	/	/	/	/	/	3.76
	B33-1/R	/	1.71	/	/	/	3.76
	B21-2/R	/	1.61	/	/	/	/
B34-1/R	B21-1/R	/	1.61	2.58	/	/	/
	B08-1/R	/	/	2.64	/	/	/
	B15-1/R	/	/	2.64	2.93	/	/
	B33-1/R	/	/	2.64	2.93	/	/
	B21-2/R	/	1.61	2.58	/	/	/
B34-1/T	B21-1/R	1.51	/	/	/	/	/
	B08-1/R	1.51	1.66	2.54	/	3.56	/
	B15-1/R	/	/	2.54	3.03	3.52	3.86
	B33-1/R	/	1.66	2.54	3.03	3.47	/
	B21-2/R	1.51	1.66	/	/	3.52	/
Mean		1.47	1.64	2.53	2.98	3.52	3.79

Ertan Dam were close to one another. The identified resonant frequencies for the PuGe and WenChuan earthquakes were approximate. The water level for the two seismic events was also approximate. The same phenomenon was observed in DaYao, YanYuan, and PanZhiHua earthquakes. It indicated that the stiffness of the dam system was almost unchanged between 2002 and 2008.

As reported in the literature [2–10,22], the resonant frequencies of arch dams initially increase with rising water level and then decrease with a further rise after a certain water level has been reached. The critical water level is approximately 70% of dam height. The resonant frequency of the Ertan Dam decreases with the increase in the water level in the reservoir. The lowest water level in the Ertan Dam for the five seismic events exceeded 80% of the dam height. Therefore, this finding coincides with the law cited in the literature.

Table 5
Resonant frequencies (Hz) identified via transfer functions for the PanZhiHua earthquake.

Input	Output	Resonant frequencies					
		Item 1	Item 2	Item 3	Item 4	Item 5	Item 6
B21-4/R	B21-1/R	1.49	/	/	/	3.32	3.58
	B21-2/R	1.49	/	/	/	/	3.58
	B08-1/R	1.49	/	/	2.49	3.42	/
B21-4/T	B21-1/R	1.44	/	2.07	2.61	/	/
	B21-2/R	1.44	/	2.07	2.61	/	/
	B08-1/R	1.44	1.51	2.22	2.61	/	/
B01-1/R	B21-1/R	1.44	/	2.00	/	3.32	3.59
	B21-2/R	1.44	/	2.00	/	/	3.59
	B08-1/R	1.44	1.49	2.17	2.32	3.32	3.58
B01-1/T	B21-1/R	1.46	/	2.00	2.66	3.49	3.64
	B21-2/R	1.46	/	2.00	2.66	3.49	3.64
	B08-1/R	1.44	/	/	2.66	3.47	/
Mean		1.45	1.50	2.07	2.60	3.42	3.59

3.4.2. Damping ratio

A credible damping ratio was only extracted with the ARX model from the records of the five earthquakes. The identified damping ratio was generally lower than 6%; in particular, this ratio was lower than 3.5% for the first three modes. This result could be attributed to the low-level seismic excitation, and it was indicative of the linear dynamic behavior of the dam. Although the identified damping ratio for a certain order mode distribute over a relatively wide range (approximately 3%), its relationship with the resonant frequency are monotone increasing or decreasing steadily, as shown in Fig. 8. However, no clear trends for the changes in the damping ratio with the resonant number appeared, and no significant variation with water level was noted.

3.4.3. Mode shape

The mode shapes of the dam were deduced with the aforementioned information. The second mode shape was estimated first. The system identification showed that the second dominant frequency could not be easily extracted from the radial component of the station located at the crown cantilever in most cases. This finding revealed the lack of radial displacement at the crown cantilever in the second-order mode shape. However, the frequency response amplitude of the other station on the crest was clear for the second dominant frequency. The second mode during the aforementioned earthquakes could be regarded as a nearly typical antisymmetric shape (Fig. 9, which shows the undeformed crest plotted for reference).

The deduction of the primary mode shape was not always easy. The primary frequency could be identified easily from the radial component of the station on the crest in most cases, except for station B15-1 during the PuGe, DaYao, and WenChuan seismic events. The phases of the frequency response at the first identified resonant frequency between the radial components of stations B21-1 and B08-1 obviously reversed during the PanZhiHua earthquake. This finding indicated the opposite radial motions of the mode shape at the two stations. Thus, the first mode seemed to be an eccentric antisymmetric shape, as shown in Fig. 10(a). However, the phases between stations B21-1 and B08-1 were the same for the PuGe event. This finding pointed to

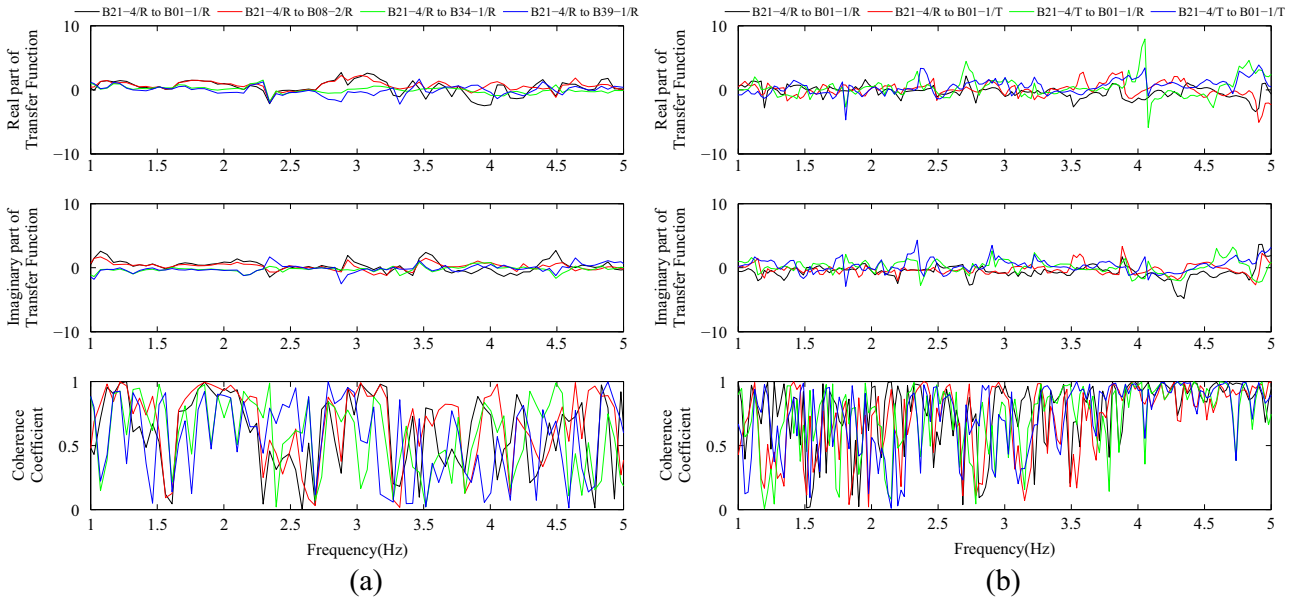

Fig. 6. Transfer functions between the records of the different stations at the abutment: (a) PuGe earthquake; (b) PanZhiHua earthquake.

another possible mode shape, that is, a mostly symmetric shape, as shown in Fig. 10(b). The two possible primary mode shapes were obviously contradictory. Moreover, the phases of the frequency response at the third identified resonant frequency between stations B21-1 and B08-1 were the same in the PanZhiHua event. Hence, the radial motions of the corresponding mode shape followed the same direction at the two stations. In general, the third mode featured an antisymmetric shape, in which the motion directions of stations B21-1 and B08-1 should be opposite. At this point, the first mode shape could not be estimated accurately. More dynamic records from strong-motion monitoring or vibration experiments (ambient vibration tests or forced vibration tests) are necessary to estimate mode shapes.

3.5. Seismic wave travel time

The seismic records are also used to compute the time delay of a wave arrival between low and high locations along dam abutments. This aspect also reflects the non-uniformity in the input ground motion. The cross-correlation between acceleration $a_n(t)$ at a high point and acceleration $a_m(t)$ at a low point is defined as follow [17]:

$$C_{n,m}(\tau) = \int_0^T a_n(t+\tau)a_m(t)dt, \quad -T < \tau < T \tag{1}$$

where T is the duration of records. The constant time delay between accelerations $a_n(t)$ and $a_m(t)$ is defined as

Table 6
Identified dynamic characteristics and computed frequencies of the five seismic events at the Ertan Dam.

Event	Water level (m)	Method	Frequency [Damping ratio] (Frequency in Hz and Damping ratio in % of critical damping)					
			Mode 1	Mode 2	Mode 3	Mode 4	Mode 5	Mode 6
WenChuan	192.4	PSD	1.59	1.68	2.46	3.08	/	3.88
		ARX	1.58[2.7]	1.67[1.7]	2.57[2.4]	3.12[3.4]	3.57[4.9]	3.90[1.7]
		Linear model	1.59	1.66	2.29	2.96	3.07	3.69
		Nonlinear model	1.63	1.66	2.34	3.03	3.15	3.77
PuGe	196.4	PSD	1.56	1.66	2.46	3.10	3.57	3.87
		TF	1.47	1.64	2.53	2.98	3.52	3.79
		ARX	1.59[1.3]	1.65[0.9]	2.49[3.2]	3.01[2.5]	3.28[4.5]	3.84[1.4]
		Linear model	1.60	1.67	2.30	2.98	3.09	3.72
		Nonlinear model	1.61	1.65	2.33	3.00	3.16	3.74
DaYao	226.8	PSD	1.42	1.54	2.25	/	2.88	3.42
		ARX	1.42[2.3]	1.51[2.3]	2.30[0.7]	2.57[3.8]	2.92[5.3]	3.34[2.5]
		Linear model	1.43	1.48	2.06	2.68	2.89	3.38
		Nonlinear model	1.44	1.48	2.09	2.71	2.95	3.39
YanYuan	228.5	PSD	1.46	/	2.34	/	2.83	/
		ARX	1.43[3.4]	1.51[2.4]	2.37[2.1]	/	2.86[2.7]	3.37[4.4]
		Linear model	1.43	1.47	2.05	2.66	2.87	3.35
		Nonlinear model	1.44	1.47	2.08	2.70	2.94	3.38
PanZhiHua	231.7	PSD	1.42	1.50	2.28	2.59	2.93	3.43
		TF	1.45	1.50	2.07	2.60	/	3.42
		ARX	1.46[1.5]	1.51[3.3]	2.18[0.8]	2.60[4.9]	2.93[5.8]	3.29[4.9]
		Linear model	1.46	1.51	2.09	2.72	2.95	3.43
		Nonlinear model	1.44	1.48	2.08	2.70	2.95	3.38

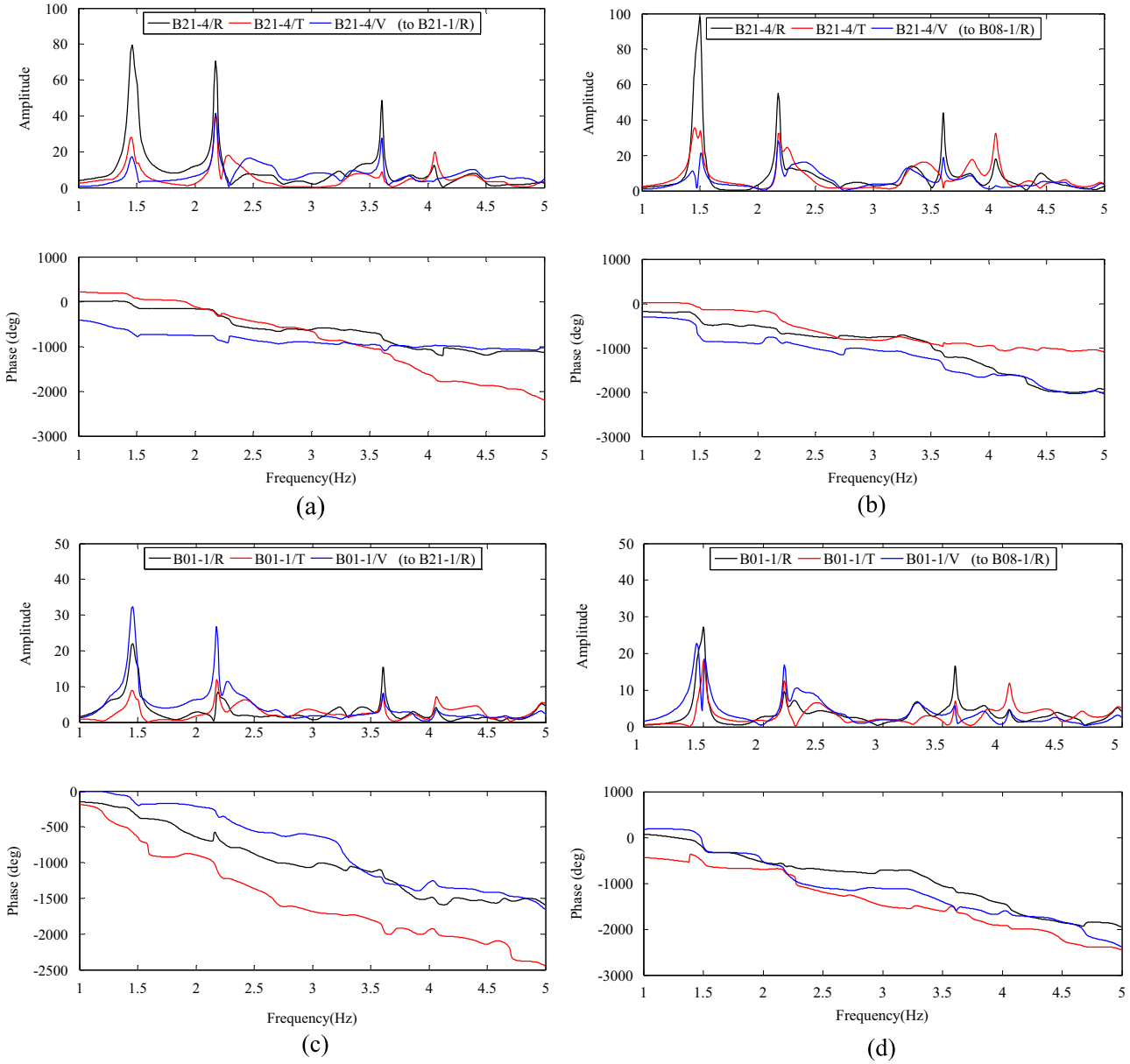

Fig. 7. Estimated frequency response functions based on the multiple input (all recorded motions along the abutment)/multiple output (radial component of stations B21-1 and B08-1) ARX model for the PanZhiHua event: (a) B21-4 as input and B21-1/R as output; (b) B21-4 as input and B08-1/R as output; (c) B01-1 as input and B21-1/R as output; (d) B01-1 as input and B08-1/R as output.

$$\tau_{n,m} = \{\tau\text{: } C_{n,m} \text{ is maximized}\} \quad (2)$$

A positive time delay indicates that the record at a high elevation lags behind the record at a low elevation. The computed time delays in the present work are listed in Table 7. According to the calibration presented in the next section, the compression and shear wave velocities for the foundation rock were approximately 4200 and 2400 m/s, respectively. Considering the elevation differences in the associated record pairs along the abutment of the dam, if the seismic waves were vertically incident body waves, the compression and shear waves would travel from 26 ms to 47 ms and from 53 ms to 93 ms. The time delay of the right abutment during the PuGe and YanYuan event ranged from 21 ms to 43 ms, which could be deemed reasonable. The same could be said for the vertical component during the WenChuan event. This result could be attributed to the recording of predominantly compression waves. During the PanZhiHua event, the tangential and vertical components at the high elevation lagged behind the accelerations at the lower elevation by 90 ms. The result could be explained by the shear wave dominating the component of the dam motion. These delays made up a significant fraction of the fundamental period of the dam (about 650 ms). However, near-zero and negative computed constant time delays were also observed. According to the concept of constant time delay, a negative time delay implies that the record at a high elevation lags before the record at a low elevation. For instance, the radial component on the left abutment leaded the radial component at the base during the PanZhiHua event. It seemed that the seismic waves propagated from up to down. Vertical component during DaYao and horizontal component during WenChuan showed simultaneous arrival of the seismic wave. Similar abnormal phenomena have been reported in ground motions recorded at the Pacoima Dam [17] and the Mauvoisin Dam [29]. No acceptable interpretation has been proposed. It indicates that the propagation of seismic wave is quite complex and extended beyond the simple concept of constant time delay.

4. Finite element modal analysis

Finite element modal analysis was performed with a linear model

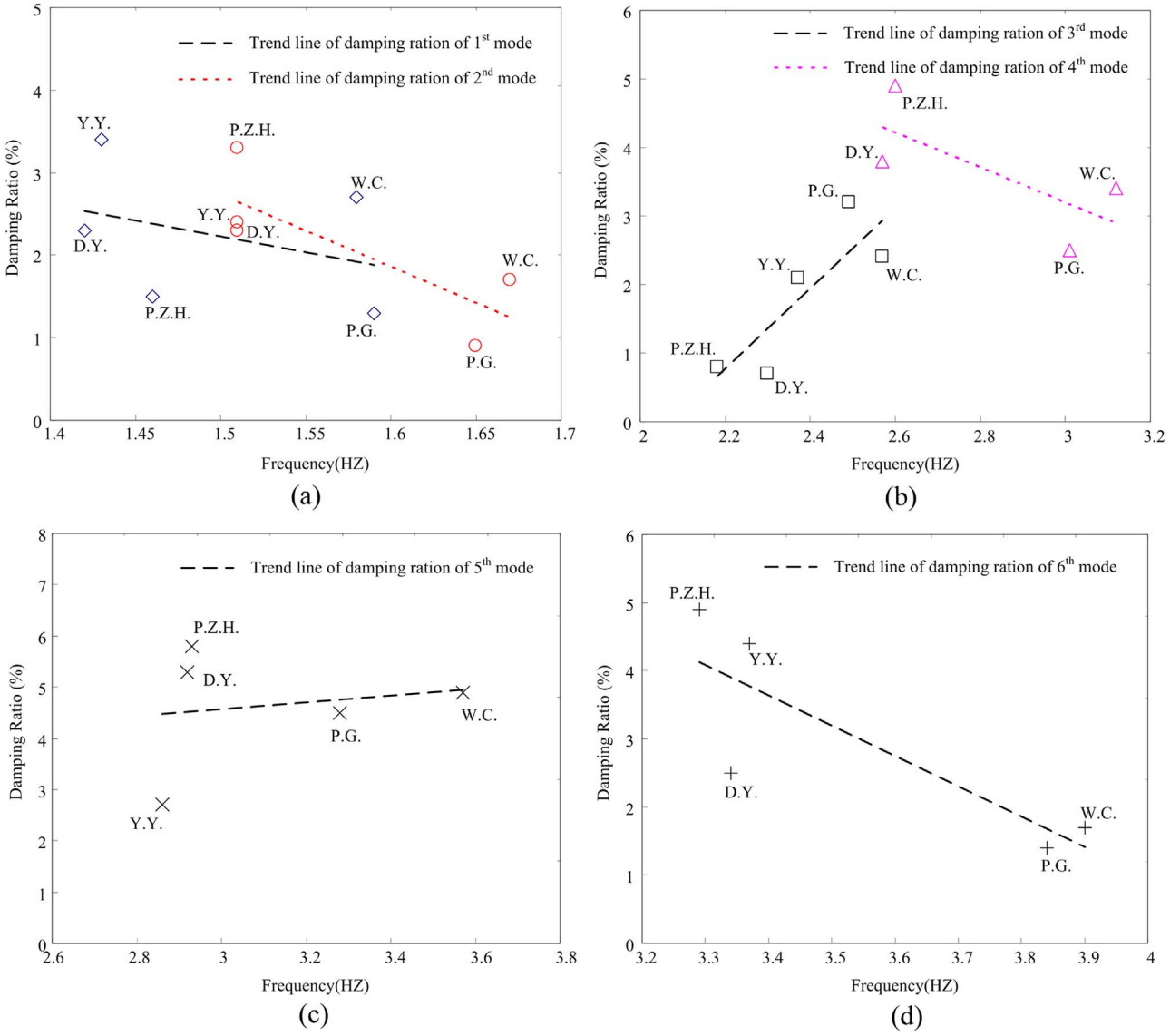

Fig. 8. Plots of the identified damping ratios with respect to the identified resonant frequencies: (a) 1st and 2nd mode; (b) 3rd and 4th mode; (c) 5th mode; (d) 6th mode.

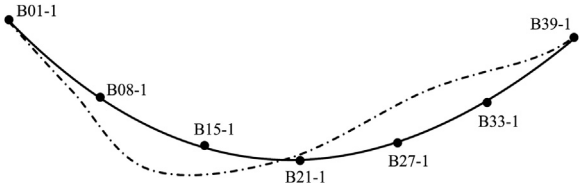

Fig. 9. Estimated second mode shape for the horizontal crest level in plan view.

and a nonlinear model with contraction joints respectively. A massless rock foundation was considered. Dam–reservoir interaction was considered for a diagonalized consistent finite element added mass matrix that represented the incompressible water impounded in the reservoir proposed by Fenves et al. [30].

4.1. Contraction joint contact model

The interaction between contraction joints was determined with an improved contact boundary model [31]. The contact boundary for the general contact consisted of master and slave surfaces. The contact relation was described with the relative position and normal stiffness matrix between the master surface and the slave surface, as shown in Fig. 11(a). The following piecewise linear function was implemented in the model to describe the pressure–overclosure relationship (Fig. 11(b)).

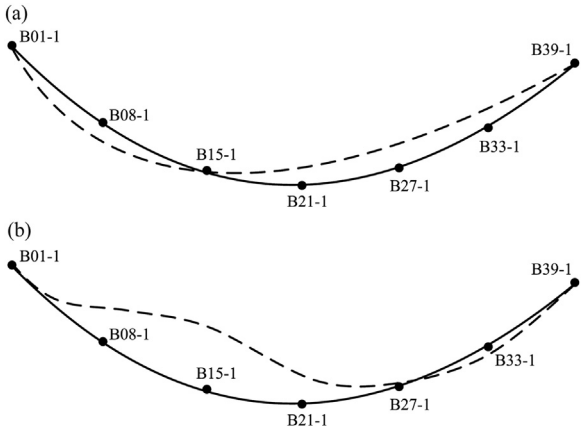

Fig. 10. Possible first mode shape for the horizontal crest level in plan view.

Table 7
Constant time delays computed from adjacent record pairs along the abutment of the dam for each component.

Event	Record pair	Elevation difference (m)	Constant time delay component (ms)[a]		
			Radial	Tangential	Vertical
PuGe	B21-4 to B08-2	111	−10	79	−12
	B08-2 to B01-1	113.75	1	1	−1
	B34-1 to B39-1	113.75	29	43	27
DaYao	B34-1 to B39-1	113.75	10	20	1
YanYuan	B34-1 to B39-1	113.75	32	38	21
WenChuan	B34-1 to B39-1	113.75	5	10	26
PanZhiHua	B21-4 to B01-1	224.75	−36	92	85

[a] A positive time delay indicates that the record at a high elevation lags behind the record at a low elevation.

$$p = \begin{cases} 0 & (h \le c_0) \\ p_0 + K_i h & (c_0 < h < 0) \\ p_0 + K_f h & (h \ge 0) \end{cases} \quad (3)$$

where c_0 is an initial overlap and p_0 is the critical pressure value at zero overlap (h=0). Linear elastic springs for tangential constraint were introduced in the model to simulate the shear keys in the arch dam, as shown in Fig. 11(c). For simplicity, no-slip occurrence was considered. Thus, the stiffness of the tangential springs, namely, K_s and K_t, was assigned a sufficiently large value. More details on contact boundary model could be refer to Ref. [31].

4.2. Finite element model and material parameters

The finite element mesh corresponding to the real geometry of the Ertan Arch Dam and site topography was constructed, as shown in Fig. 12. The dam body and foundation comprised 7500 and 66,800 isoparametric brick elements, respectively. The water mesh extended upstream about thrice the dam height. The foundation mesh extended horizontally twice the dam height away from the left abutment, twice the upstream and thrice the downstream of the dam at the dam–foundation interface. The 38 contraction joints in the nonlinear model (Fig. 12(b)) were approximated to those in the original design. For each joint, the initial clearance c_0=1 mm, and the normal stiffness of the contact boundary K_i=5 GPa/m and K_f=50 GPa/m. The tangential spring stiffness values, namely, K_s and K_t, were set to 1×10^9 kN/m. The nonlinear representation was simplified into a linear one after removing the joints. Thus, the element discretization of the linear model was the same as that of the nonlinear model, except that the number of dam body nodes was reduced from 13,552 to 9282 through the combination of dual nodes at the contraction joints. The thermal and mechanical properties of the dam concrete and rock (Table 8) were acquired from previous studies [32,33]. The water level was assumed to be the actual water level in Table 2, except in special notations.

4.3. Modal analysis

Self-weight, thermal and hydrostatic loads were all included in calibrating the two finite element models to obtain the real performance of the dam. The thermal load used was obtained from previous studies [32,34], and the reference temperature for the zero stress conditions was taken from the time of contraction joint grouting. The E_d values (dynamic elastic modulus) for the concrete and rock were synchronously adjusted in the calibration to reproduce the frequencies determined from the aforementioned system identification. For convenience, a coefficient η was introduced to denote the ratio of the dynamic and static elastic moduli, that is, $\eta=E_d/E_s$. The resulting frequencies through calibration are listed in Table 6, and the corresponding coefficient for every seismic event is listed in Table 9.

The coefficient calibrated with the linear model distributed over a large range, that is, from 1.10 to 1.23. Supposing the largest coefficient belonging to the PanZhiHua earthquake was attributed to the strongest dynamic response of the dam, the coefficient of the WenChuan event was smaller than that of the PuGe event with respect to the approximate water level. However, the dynamic response of the dam during the WenChuan event was considerably stronger than that during the PuGe event. Moreover, the linear model resulted in a nearly antisymmetric shape as the first mode and a mostly symmetric shape as the second mode. This result is far from the aforementioned discussion on mode shapes. Interestingly, the coefficient obtained from the nonlinear model was nearly constant (approximately 1.30) for the five seismic events, regardless of when the earthquakes occurred, how strong the earthquakes were, and how high the water levels were. The second mode shape computed from the nonlinear finite element model was antisymmetric (Fig. 13(b)), which coincides well with the result of the system identification. The primary mode from the nonlinear model was symmetric (Fig. 13(a)), which matches the second possible mode shape.

The actual reservoir level of the Ertan Dam normally ranges from 50 m below the crest in summer to 5 m below the crest in winter. The lowest water level was higher than the mentioned critical turning point.

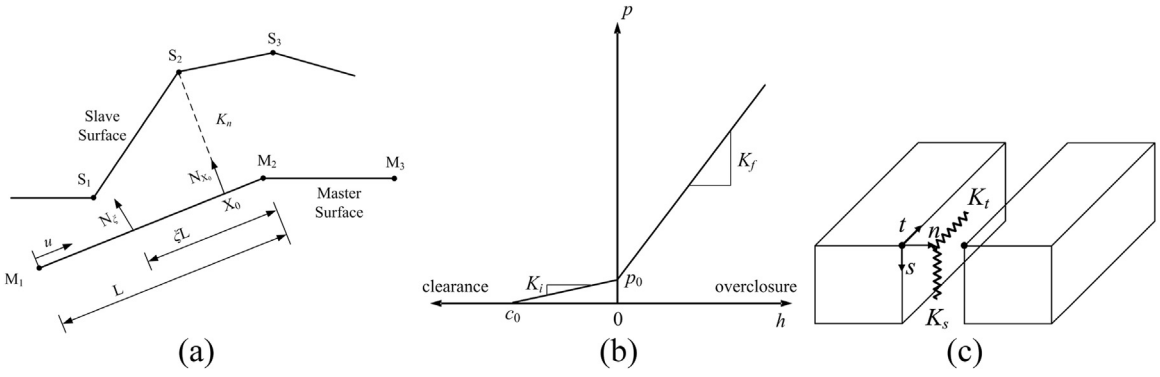

Fig. 11. Contraction joints contact model: (a) contact relation; (b) pressure–overclosure constitutive; (c) tangential springs.

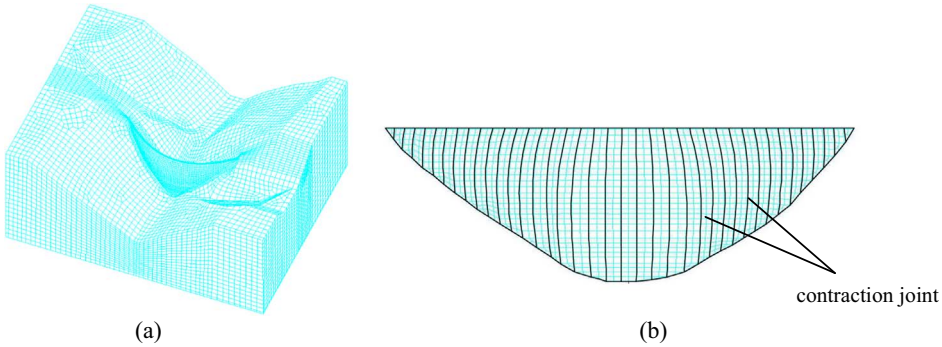

Fig. 12. Finite element discretization of the Ertan Dam: (a) dam and foundation rock; (b) dam contraction joints.

Table 8
Material properties of concrete and rock.

Property	Dam concrete	Rock
Static elastic modulus, E_S (GPa)	35	32.5
Mass density, ρ (kg/m^3)	2400	/
Poisson's ratio, ν	0.17	0.25
Thermal expansion coefficient, α (1/ °C)	8.01×10^{-6}	1×10^{-5}

Table 9
Ratio of dynamic and static elastic moduli (the coefficient η) through calibration.

Event	W.C.	P.G	D.Y.	Y.Y.	P.Z.H.
Linear model	1.10	1.13	1.13	1.13	1.22
Nonlinear model	1.30	1.30	1.30	1.30	1.35

A numerical experiment with the assumed low water levels (Table 10) was conducted to investigate the variation in the resonant frequencies with the water level of the arch dam. For convenience, the coefficient η, that is, the ratio of the dynamic and static elastic moduli, was assumed uniform at 1.13 and 1.30 for the linear and nonlinear models, respectively.

Fig. 14 presents the comparison of the computed and identified resonant frequencies. The resonant frequencies computed with the linear model steadily decreased with the rising water level because of the increase in the added water masses. Together with the conjunction joints, the nonlinear model confirmed the tendency of the resonant frequencies of the arch dam to initially increase with the rising water level and then decrease with a further rise after a certain water level has been reached. This finding was also presented by several previous studies [2–10,22]. This phenomenon could be attributed to an increase in the stiffness of the dam caused by the compression of the construction joints under increasing hydrostatic pressure. After a certain water level was reached, this phenomenon was overcame by the added mass of the reservoir, and the resonant frequencies began to decrease. The certain water level was approximately 0.7 times the height of the Ertan Arch Dam. Meanwhile, the variation in the computed mode shape with the water level also followed regularity, as shown in Table 10. The primary mode showed an antisymmetric shape, and the second mode showed a mostly symmetric shape when the water level was relatively low. After reaching the particular water level, the mode shapes transformed between the fundamental two modes.

Table 10
Mode shape obtained from the numerical analysis with the nonlinear model (the symbol S and A respectively denote symmetric and antisymmetric mode shape.).

Water level, H (m)	100	122	150	178	192.4	196.4	226.8	228.5	231.7
Ratio, H/H_s	0.417	0.508	0.625	0.742	0.802	0.818	0.945	0.952	0.965
First mode shape	S	A	A	S	S	S	S	S	S
Second mode shape	A	S	S	A	A	A	A	A	A

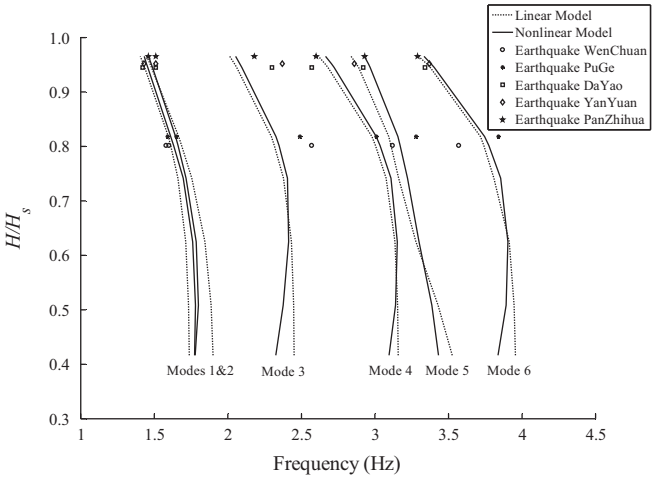

Fig. 14. Comparison of computed and identified resonant frequencies.

5. Conclusion

This paper presents the system identification of the Ertan Arch Dam

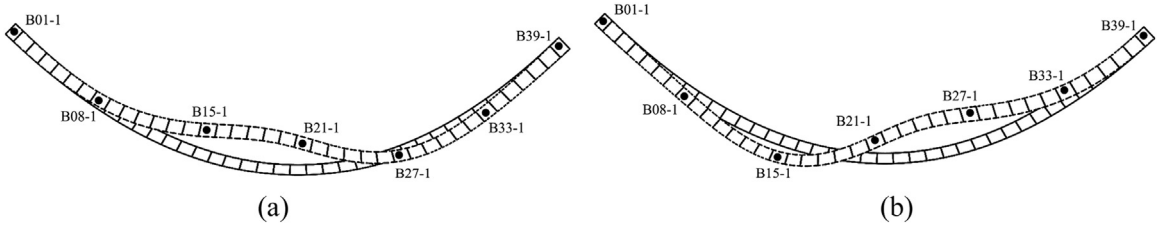

Fig. 13. Mode shapes computed from the nonlinear finite element model: (a) first mode, symmetric; (b) second mode, antisymmetric.

based on seismic response data recorded by the strong-motion instrumentations in the dam. The records for the top five strongest earthquakes from 2002 to 2008, namely, the PuGe, DaYao, YanYuan, WenChuan, and PanZhiHua earthquakes, were selected for system identification. Despite the slight differences, the dynamic characteristics identified with different methods (PSD functions, TFs, and ARX model) were generally the same for a certain earthquake. This work is beneficial for the conduct of seismic safety analysis and earthquake-resistant design.

The identified resonant frequency of the Ertan Dam decreased with the increase in the water level in the reservoir. The two fundamental resonant frequencies were always close to each other. The identified resonant frequencies were approximate for the different seismic events if the water level was approximate. This finding indicates that the stiffness of the dam system was stable between 2002 and 2008. The non-uniformity in the input ground motion was noted through identification. It was also provided by the computed time delay of the wave arrival between the low and high locations along the abutment. However, the records of the stations along the abutment, which were partly lost in most of the seismic events because of the fault in the strong-motion instrumentation, were contaminated to a certain degree by the dam–rock interaction. Thus, some potential errors resulting from the hypothesis and/or approximation would be introduced in the generation of the spatially non-uniform excitation for the numerical analysis.

A credible damping ratio was extracted only with the ARX model because of the noise component of the records and the low resolution of the frequency response function. The linear dynamic behavior of the dam in the seismic events was obvious because the identified damping ratio was generally lower than 3.5% for the first three modes. This finding may be mainly attributed to the low-level seismic excitation. No clear trend was observed in the changes of the damping ratio with the resonant number, as well as with the water level.

Some difficulties were encountered in the deduction of the primary mode shape. Two contradictory shapes, an eccentric antisymmetric shape and a mostly symmetric shape, were possible for the primary mode according to the system identification. In consideration of the subsequent modal analysis, the mostly symmetric shape may be preferred to the first mode. The second mode in these seismic earthquakes could be concluded as a nearly typical antisymmetric shape. Dynamic records from strong- motion monitoring or vibration experiments are suggested to confirm the mode shape.

A linear finite element model of the dam and a nonlinear model with contraction joints were compared. The dynamic elastic modulus of the dam concrete and rock calibrated by the nonlinear model was nearly constant for the five seismic events. This observation was consistent with the stability of the stiffness of the dam system during the given periods. The shapes computed from the nonlinear model were symmetric and antisymmetric for the primary and second modes, respectively. This result logically matched that of the system identification. By extending the modal analysis further, the nonlinear model was found to reproduce the tendency of the resonance frequencies of the arch dam to initially increase with the rising water level and then decrease with a further rise after a certain water level based on some virtual water level. Compared with the poor performance of the linear model, the nonlinear model should be reasonable in simulating the dynamic response of the Ertan Arch Dam.

Acknowledgements

This research was supported by grants from the National Natural Science Foundation of China (no. 41274106 and 51179093). The authors are grateful to Yalong River Hydropower Development Company, Ltd. for authorizing the use of the earthquake motions recorded at Ertan Dam. Appreciation is also expressed to Dr. Erol Kalkan of the United States Geological Survey for preprocessing the earthquake motion records.

References

[1] Hall JF. The dynamic and earthquake behaviour of concrete dams: review of experimental behaviour and observational evidence. Soil Dyn Earthq Eng 1988;7(2):58–121.
[2] Fanelli MGiuseppetti GBettinali FGalimberti CCastoldi ACasirati M. Seismic monitoring of dams a new active surveillance system: basic criteria, operating methods and results obtained. In: Proceedings of the ninth world conference on earthquake engineering; 2008. p. 409–14.
[3] FanelliMGiuseppettiGCastoldiABonaldiP. Dynamic characterization of Talvacchia Dam: Experimental activities, numerical modeling, monitoring. In: Proceedings of the tenth worldconference on earthquake engineering, Madrid; 1992. p. 2689–94.
[4] Loh C-H, Wu T-S. Identification of Fei-Tsui arch dam from both ambient and seismic response data. Soil Dyn Earthq Eng 1996;15(7):465–83.
[5] Loh C-H, Wu T-C. System identification of Fei-Tsui Arch Dam from forced vibration and seismic response data. J Earthq Eng 2000;4(4):511–37.
[6] Darbre GR, de Smet CAM, Kraemer C. Natural frequencies measured from ambient vibration response of the arch dam of Mauvoisin. Earthq Eng Struct Dyn 2000;29(5):577–86.
[7] Darbre GR, Proulx J. Continuous ambient-vibration monitoring of the arch dam of Mauvoisin. Earthq Eng Struct Dyn 2002;31(2):475–80.
[8] Proulx J, Paultre P, Rheault J, Robert Y. An experimental investigation of water level effects on the dynamic behaviour of a large arch dam. Earthq Eng Struct Dyn 2001;30(8):1147–66.
[9] Mendes P, Costa CO, Garrett JA, Oliveria S. Development of a monitoring system to Cabril Dam with operational modal analysis. In: Proceedings of the 2nd experimental vibration analysis for civil engineering structures (EVACES); 2007.
[10] Okuma N.Etou Y.Kanazawa K.Hirata K. Dynamic properties of a large arch dam after forty-four years of completion. In: Proceedings of the 14th world conference on earthquake engineering; 2008.
[11] Darbre GR. Strong-motion instrumentation of dams. Earthq Eng Struct Dyn 1995;24(8):1101–11.
[12] Darbre GR. Strong-motion records at large dams. In: Proceedings of the 12th world conference on earthquake engineering: Auckland; 2000.
[13] Proulx J, Darbre GR. Modeling damping for seismic safety evaluation of arch dams. Int J Hydropower Dam 2003;10(2):110–3.
[14] Proulx JDarbre GRKamileris N. Analytical and experimental investigation of damping in arch dams based on recorded earthquakes. In: Proceedings of the 13th world conference on earthquake engineering; 2004.
[15] Bell DKDavidson BJ. Response identification of Pacoima dam for the 1994 northridge earthquake. In: Proceedings of the 11th world conference on earthquake engineering; 1996.
[16] Alves SW, Hall JF. System identification of a concrete arch dam and calibration of its finite element model. Earthq Eng Struct Dyn 2006;35(11):1321–37.
[17] Alves SW, Hall JF. Generation of spatially nonuniform ground motion for nonlinear analysis of a concrete arch dam. Earthq Eng Struct Dyn 2006;35(11):1339–57.
[18] Zhang L, Xing G, Zhang M. Earthquake analysis of Longyangxia gravity arch dam. Water Power 1998;12:14–7, [in Chinese].
[19] MojtahediSFenvesGL. Response of a concrete arch dam in the 1994 Northridge, California earthquake. In: Proceedings of the 11th world conference on earthquake engineering; 1996.
[20] Tarinejad R, Fatehi R, Harichandran Ronald S. Response of an arch dam to non-uniform excitation generated by a seismic wave scattering model. Soil Dyn Earthq Eng 2013;52:40–54.
[21] Wang R, Shao J. Shapai arch dam has withstood Wenchuan earthquake beyond fortification level. J Hydroelectr Eng 2009;28(5):92–6, [in Chinese].
[22] Okamoto S. Introduction to earthquake engineering, 2nd ed.. Tokyo: University of Tokyo Press; 1984.
[23] Fujii T, Egawa K, Katayama I. Dynamic behavior of Nagawado Arch Dam in the event of 1984 Naganoken Seibu Earthquake. Earthq Spectra 1987;3(2):347–64.
[24] Ariga YWatanabe H. Reproduction analysis of real behavior existing arch dam during the 1995 Hyogoken-Nanbu earthquake. In: Proceedings of the 13th world conference on earthquake engineering; 2004.
[25] Hansen KD, Roehm LH. The response of concrete dams to earthquakes. Water Power Dam Constr 1979;31(4):27–31.
[26] Castoldi A. New criteria for the seismic monitoring of dams: A dynamic active surveillance system. In: Proceedings of Joint China-U.S., Workshop on earthquake behavior of arch dams; 1987.
[27] Serafim JL. A Note on the Earthquake Performance of Arch Dams. In: Proceedings of Joint China-U.S., Workshop on earthquakke behavior of arch dams, 1987.
[28] Bailin Tang, Mingzhu Guo, Jihuan Wang. Strong earthquake station of arch dam for Ertan Hydro-electric power factory. World Earthq Eng 2006;22(3):156–9, [in Chinese].
[29] Wang J, Chopra AK. Linear analysis of concrete arch dams including dam-water-foundation rock interaction considering spatially varying ground motions. Earthq Eng Struct Dyn 2010;39:731–50.
[30] FenvesGLMojtahediS. Reimer RB. ADAP-88, A computer program for nonlinear earthquake analysis of concrete arch dams. Report No. 89/12. Earthquake engineering research center, University of California at Berkeley; 1989.
[31] Zhang C, Pan J, Wang J. Influence of seismic input mechanisms and radiation on arch dam response. Soil Dyn Earthq Eng 2009;29(9):1282–93.
[32] Jin F.Yang J.Wang J. A primary digital dam simulation system for an arch dam. In: Proceedings of the 1st international conference on long time effects and seepage behavior of dams; 2008. p. 13–22.
[33] Ertan Hydropower Development Company Ltd. Project summary of ertan hydropower plant. Beijing: China waterpower press; 2005. [in Chinese].
[34] Jin F, Chen Z, Wang J, Yang J. Practical procedure for predicting non-uniform temperature on the exposed face of arch dams. Appl Therm Eng 2010;30(14–15):2146–56.